The Astrophysical Journal, 736:158 (14pp), 2011 August 1 doi:10.1088/0004-637X/736/2/158

CHANDRA AND *HST* STUDIES OF THE X-RAY SOURCES IN GALACTIC GLOBULAR CLUSTER M92

Ting-Ni Lu[1], Albert K. H. Kong[1,7], Frank Verbunt[2,3], Walter H. G. Lewin[4], Scott F. Anderson[5], and David Pooley[6]
[1] Institute of Astronomy & Department of Physics, National Tsing Hua University, Taiwan
[2] Astronomical Institute, Utrecht University, P.O. Box 80000, 3508 TA Utrecht, The Netherlands
[3] SRON Netherlands Institute for Space Research, Sorbonnelaan 2, 3584 CA Utrecht, The Netherlands
[4] Kavli Institute for Astrophysics and Space Research, Massachusetts Institute of Technology, 77 Massachusetts Avenue, Cambridge, MA 02139, USA
[5] Department of Astronomy, University of Washington, Box 351580, Seattle, WA 98195, USA
[6] Eureka Scientific, Inc., Austin, TX 78756, USA
Received 2011 February 12; accepted 2011 May 24; published 2011 July 19

ABSTRACT

We present the analysis of two observations of M92 taken with the *Chandra X-Ray Observatory*. We combined the two data sets with a total exposure of ∼52 ks. With the combined observation, we detected 10 X-ray sources inside the half-mass radius (1.′02), five of which are inside the core radius (0.′26) of M92. The luminosities of the 10 sources are roughly within the range of 10^{30}–10^{32} erg s^{-1} assuming cluster memberships. The background estimation suggests 7–8 cluster members and 2–3 background galaxies in M92. We identified the 10 sources by using *Hubble Space Telescope* Advanced Camera for Surveys observations of M92. Based on the X-ray and optical characteristics, we classified 4–5 possible candidates for cataclysmic variables within the half-mass radius. We discussed the possible formation mechanisms of the X-ray sources in M92 by comparing the predicted X-ray source number and observational results. Under the assumption that the number of X-ray sources scales with the encounter rate and the mass of the globular cluster, we expected eight X-ray sources formed from dynamical interactions and four from primordial binaries inside M92, which is consistent with the background estimation and comparable with the observational results. We therefore suggest that the X-ray sources in M92 may be contributed from both dynamical origin and primordial binaries.

Key words: globular clusters: individual (M92)

Online-only material: color figures

1. INTRODUCTION

Due to their high stellar density and frequent stellar interactions, globular clusters (GCs) are more efficient at producing exotic binary systems than the Galactic plane. For example, bright X-ray sources (with X-ray luminosity $L_X \gtrsim 10^{36}$ erg s^{-1}) are overrepresented by two orders of magnitude in GCs with respect to the Galactic disk when we compare by the mass in ordinary stars (Katz 1975; Clark 1975). The binary content of GCs can be efficiently investigated by studying their population of X-ray sources. The primordial binary population is a key ingredient in the evolution history of GCs. Thus, studying the population of X-ray sources in GCs can not only help us understand more about the physical properties of X-ray binaries and their formation mechanism, but also helps us construct the dynamical evolution scenario of GCs (Hut et al. 1992). Numerical modeling techniques can provide direct predictions of the current binary population from the primordial fraction in GCs (e.g., Hurley et al. 2007). On the other hand, the X-ray binary population could be constrained by observations. Observations of X-ray bursts from the bright X-ray sources in GCs showed that they are binary systems containing a neutron star, and early theoretical work showed that these are formed through stellar interactions like tidal capture or exchange encounters (Fabian et al. 1975; Hills 1976).

As for the low-luminosity X-ray sources ($L_X \lesssim 10^{34.5}$ erg s^{-1}), the population was first investigated by Hertz & Grindlay (1983). With the high resolution (down to the scale of subarcsecond) and much better sensitivity of the *Chandra X-Ray Observatory* and *Hubble Space Telescope* (*HST*), the faint X-ray sources in GCs could be identified in detail. These dim sources consist of various types of X-ray binary systems. The brightest are quiescent low-mass X-ray binaries (qLMXBs, an accreting neutron star or black hole with a companion star at a low accretion rate), and then cataclysmic variables (CVs, an accreting white dwarf with a main-sequence or subgiant companion), followed by active binaries (ABs, two main-sequence/subgiant objects in a binary), and millisecond pulsars (MSPs) which are thought to be the descendants of the LMXBs with X-ray luminosities similar to those of CVs. Theory predicts different formation mechanisms for various X-ray sources in GCs: (1) low-luminosity X-ray sources containing a neutron star, and their descendants, millisecond radio pulsars, are formed in GCs mainly via stellar encounters and their numbers scale with the total encounter rate of a cluster; (2) X-ray ABs are mostly primordial binaries, so that their numbers scale with the total mass of the cluster; and (3) CVs may arise both via evolution of primordial binaries (in clusters with low number density of stars) and via stellar encounters (in clusters with a high central number density of stars; Verbunt 2002).

Chandra and *HST* have been used extensively to investigate the population of dim X-ray sources among ∼15 Galactic GCs. They include 47Tuc (Grindlay et al. 2001; Edmonds et al. 2003; Heinke et al. 2005), NGC 6397 (Grindlay et al. 2002; Cohn et al. 2010), ω Centauri (Rutledge et al. 2002), NGC 6752 (Pooley et al. 2002b), NGC 6440 (Pooley et al. 2002a), NGC 6626 (Becker et al. 2003), M4 (Bassa et al. 2004), NGC 288 (Kong et al. 2006), NGC 2808 (Servillat et al. 2008), M55, NGC 6366 (Bassa et al. 2008), M12 (Lu et al. 2009), M71 (Huang et al. 2010), and E3 and NGC 6144 (Lan et al. 2010). Pooley & Hut (2006) and Bassa et al. (2008) use the numbers of X-ray sources with luminosity $L_X > 4 \times 10^{30}$ erg s^{-1} in the 0.5–6.0 keV

[7] Golden Jade Fellow of Kenda Foundation, Taiwan.

range discovered in these observations to confirm the theoretical prediction of their origins.

M92 is a relatively low-density core GC with a core radius $r_c = 0.'26$ and a half-mass radius $r_h = 1.'02$ (Harris 1996, version of 2010 December). The distance to M92 is 8.3 kpc, its absolute visual magnitude is −8.21. These numbers give M92 an encounter rate and mass comparable to those of M4, and therefore we may expect that there would be more ABs in M92, and the number of X-ray sources would therefore have a stronger dependence on the total mass. M92 is well above the Galactic disk ($l = 68.°34$, $b = 34.°86$) so there are not as many foreground/background stars in this region as there are on the Galactic disk, and the interstellar extinction is low: $E[B-V] = 0.02$, corresponding to a neutral hydrogen column density $N_H = 1.06 \times 10^{20}$ cm^{-2} (derived from $N_H = 5.3 \times 10^{21}\, E[B-V]$ cm^{-2} by Predehl & Schmitt 1995). M92 is therefore a good target to study the correlation between the number of X-ray sources and the encounter rate, as well as the mass of GCs in the low core density regime.

Optical searches for binaries in M92 hitherto have been unsuccessful. Shara et al. (1994) detected no dwarf novae in a ground-based study limited by crowding to the outer regions of the cluster ($r > 6r_c$). Kopacki (2001) studied variable stars and found that all of them are pulsational variables, predominantly RR Lyr variables; they also summarize and discuss earlier searches for variable stars in M92.

The first detection of an X-ray source in M92 was made by Johnston et al. (1994) with the *ROSAT* Position Sensitive Proportional Counter (PSPC), and confirmed by Fox et al. (1996) with the *ROSAT* High-Resolution Imager (HRI). The *ROSAT* HRI observation also detects the W UMa variable V798 Her, unrelated to the cluster, which was used by Geffert (1998) to determine the boresight correction, which turned out to be surprisingly large, about 14″. This correction leads to a further identification of *ROSAT* source 6 with a star in the TYCHO catalog, presumably a G star. Ferraro et al. (2000) ignored this correction and thereby wrongly identified an ultraviolet object detected in an *HST* WFPC2 observation with the X-ray source in the core of M92. A re-analysis with the improved *ROSAT* software by Verbunt (2001) gives positions of the X-ray sources near M92 different from those of the earlier analyses, and confirms the boresight correction made by Geffert (1998). Verbunt (2001) further shows that the source in M92 is variable, being about 6.5×10^{32} erg s^{-1} in 1992 August, and about 2.4×10^{32} erg s^{-1} during the other four observations, in April 1992 and in 1994 and 1995. If the X-ray spectrum of the *ROSAT* PSPC source is fitted with a bremsstrahlung spectrum with absorption column fixed to 10^{20} cm^2, the fit is not acceptable; only with an absorption column higher by a factor 2.5 is an acceptable fit found, with $kT \simeq 1.1$ keV. As we will see below, the *ROSAT* source corresponds to the brightest source found with *Chandra* (CX1), possibly with some contribution by CX2.

In Section 2, we describe the observation and analysis of *Chandra* X-ray data. The *HST* optical data is presented in Section 3. In Section 4, we discuss the source identification and in Section 5 compare our results with other GCs.

2. X-RAY OBSERVATIONS AND ANALYSIS

M92 was observed on 2003 October 5 and 19 for 30 ks and 23 ks with the Advanced CCD Imaging Spectrometer (ACIS) on the *Chandra X-Ray Observatory* with ObsID 3778 and 5241, respectively. The telescope aim point is on the ACIS back-illuminated S3 chip. The data were taken in the timed mode with a frame transfer time of 3.24 s and were telemetered to the ground in faint mode. The field of view (FOV) of ACIS S3 chip ($\sim 8.'3 \times 8.'3$) covering the whole half-mass radius of M92. In this paper, we only consider the data taken with the S3 chip.

2.1. Data Reduction

We used CIAO, version 3.4 provided by the *Chandra* X-Ray Center (CXC)[8] to perform data reduction and analysis. We reprocessed the level 1 event files with CALDB, version 3.4.2. The reprocessing included flagging and filtering out the cosmic rays and creating a new bad-pixel file by using `acis_run_hotpix` package. The data were also filtered with the Advanced Satellite for Cosmology and Astrophysics grades of 0, 2, 3, 4, and 6 which are the standard values to optimize the instrumental signal-to-background ratio. We only processed the events extracted with photon energies in the range of 0.3–7 keV. Periods of high background flares (count rate >4 counts s^{-1} estimated from inspection of the entire area of chip S1) were eliminated for both data sets. The final effective exposure time was 29.6 ks and 22.8 ks for the 3778 and 5241 observations, respectively. We then combined the two data sets by using `merge_all` package and created an exposure map for the merged data set. The merged data set then has an effective exposure time of 52.5 ks.

2.2. Source Detection

We employed the CIAO package `wavdetect` to detect X-ray sources. The source detections were performed on data sets 3778, 5241, and the combined data sets. For the three data sets, we set the wavelet scales (also the sizes of the point-spread function, PSF) to be a series from 1 to 16 increasing by a factor of $\sqrt{2}$. We also set the detection signal threshold to be 10^{-6} such that there will be at most one false detection (fake source) caused by background fluctuation. We performed `wavdetect` with exposure maps in the total energy band (0.3–7 keV). The data were divided into three energy bands: soft band (0.3–1 keV), medium band (1–2 keV), and hard band (2–7 keV). We extracted photon counts in the three sub-bands with the source regions that were created by the source detection in the total energy band. We then produced a master source list based on the combined data set. We detected 39 sources in the whole ACIS-S3 chip and 10 of them are inside r_h of M92. Source 10, 28, 38, and 39 were only detected in the combined data, not in the 3778 or 5241 observations. Figure 1 shows the resultant sources on the merged S3 chip. Table 1 lists the information of the 39 sources ordered by increasing unabsorbed flux within 0.3–7 keV, separately for sources within the core and outside the core. The columns list the source name, the position of the source (J2000.0), the net counts (source counts excluding the background contribution) in the three bands (X_{soft}, X_{medium}, and X_{hard}), the unabsorbed flux within 0.3–7 keV and 0.5–2.5 keV, indication of the presence of optical counterparts, and the applicable *ROSAT* counterpart. The photon counts from the three bands were extracted from the source region corresponding to the 3σ `wavdetect` ellipse in the total energy band (0.3–7 keV) with the task `dmextract`. Furthermore, the background counts were extracted from an annulus centered at the individual source and outside the 3σ `wavdetect` ellipse region. The unabsorbed flux was calculated from the source count rates by assuming a power-law model with a column density $N_H = 1.06 \times 10^{20}$ cm^{-2} and a photon index of 2.

[8] See http://cxc.harvard.edu/.

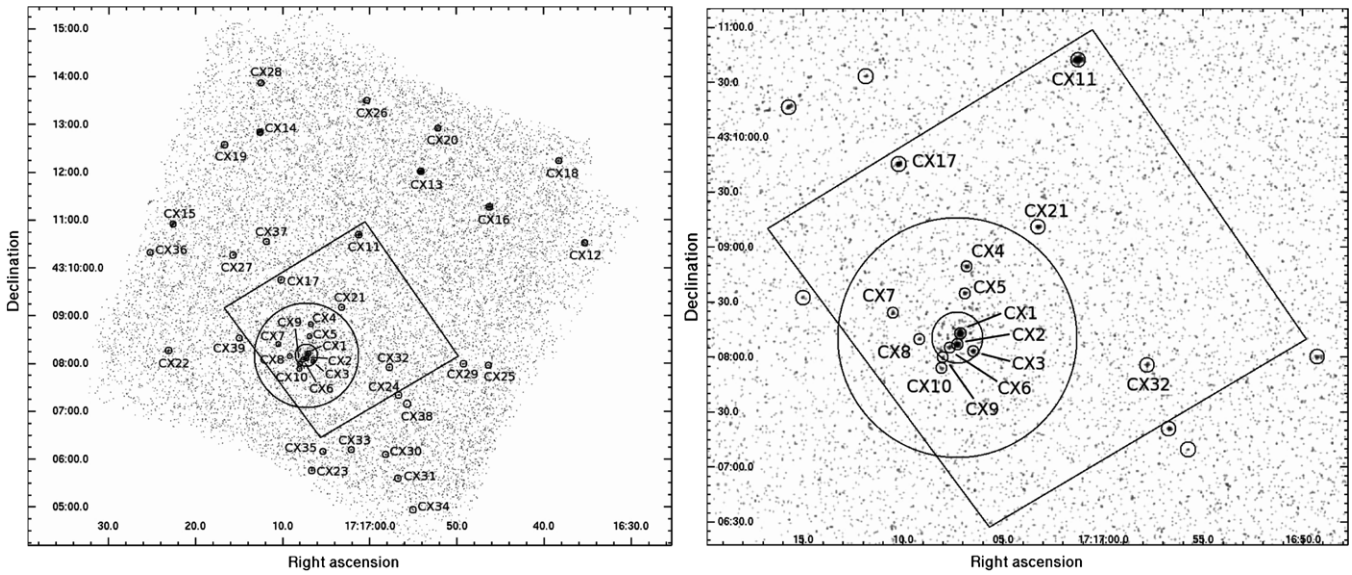

Figure 1. Merged *Chandra* ACIS-S3 0.3–7 keV image of M92. The 39 detected X-ray sources are marked and named with their CX number. The inner circle is the core radius r_c, and the large circle is the half-mass radius r_h of the globular cluster M92. The box is the FOV of the *HST* ACS drizzled image. The left panel shows the whole FOV of *Chandra* observations, while the right panel shows the central region of M92.

We estimated the background source contribution by using the log N–log S relation from the *Chandra* Deep Field Survey (Brandt et al. 2001). Sources detected in this survey are active galactic nuclei (AGNs) and distant galaxies, and therefore we took them as background sources unrelated to M92. Considering the completeness limit of the combined data, we expect 34 or 35 (not including Poisson noise) out of 39 within the ACIS-S3 chip and 2–3 out of 10 within r_h to be background (AGNs) contribution. By taking the detection limit instead of the completeness limit, we would get a similar result that ∼3 sources are background objects within r_h. The background contribution can also be estimated by scaling the number of X-ray sources outside r_h to that inside r_h. This gives $29 \times \pi r_h^2/(r_{S3}^2 - \pi r_h^2) \approx 2$ background sources inside r_h of M92, where r_{S3}^2 is the area of ACIS-S3 chip. This is consistent with the log N–log S relation derived from the *Chandra* Deep Field Survey. For an expected number of three background sources the Poissonian probability of detecting 10 or more background sources is about 0.0011. It is therefore very unlikely that all the detected sources within r_h are background sources.

2.3. X-Ray Colors, Spectral Fitting, and Variability

Most of our detected X-ray sources are too faint to allow a spectral fit. However, we can make a rough estimate of the X-ray properties from the hardness ratio constructed from the photon counts in different energy bands. We used the CIAO tool `dmextract` to extract the photon counts, and the hardness ratio is defined as $HR1 = (X_{medium} - X_{soft})/(X_{medium} + X_{soft})$ and $HR2 = (X_{hard} - X_{soft})/(X_{hard} + X_{soft})$. The X_{soft}, X_{medium}, and X_{hard} represent the photon counts extracted from the three energy ranges, 0.3–1, 1–2, and 2–7 keV. We choose these energy ranges of the color–magnitude diagram (CMD) to be consistent with previous works (e.g., Kong et al. 2006; Bassa et al. 2008; Lu et al. 2009; Lan et al. 2010). Figure 2 shows the X-ray color–color diagram (left panel) and the CMD (right panel) of all the 39 sources detected on the ACIS-S3 chip. The four lines on the color–color diagram are the spectra predicted by a thermal bremsstrahlung model and power-law model with different column densities.

For the brightest sources ($\gtrsim$ 200 counts), we extracted the spectrum in the energy range 0.3–7.0 keV for observations 3778 and 5241 individually. We bin the data such that the number of counts per spectral bin is at least 15 and we performed simultaneous fitting for both observations 3778 and 5241. We fitted the spectrum of CX1, CX11, and CX13 with a power-law model and a thermal bremsstrahlung model. All the models for the three sources can be fitted with a reduced χ^2/degrees of freedom ∼1.5/18, 0.6/28, and 0.9/8 for CX1, CX 11, and CX13, respectively; the probability of getting a higher χ^2, if the fit is correct, is about 0.1. Table 2 summarizes the results of spectral fitting. The fitted column density for CX1 is higher than the value toward the cluster. A two-component model can improve the spectral fit, but results in an even higher column density and a higher flux. We tested the significance of adding another component in the spectral fit of CX1 with the F-test. The F-test probability is ∼4%, and the low probability suggests the additional component is reasonable. The fitted photon index is roughly 3.8 for CX1 and 1.8 for CX11, while the fitted temperature for the thermal bremsstrahlung model for CX1 is roughly 0.7 keV. We only used data set 3778 for the spectrum fitting of CX13, since it is too faint in data set 5241. CX13 cannot be fitted with a single component model with a reasonable reduced χ^2 ($\lesssim$2), and therefore we fitted its spectrum with a power-law model plus a collisional plasma model (Astrophysical Plasma Emission Code: APEC; Smith et al. 2001). Some sources show a change in flux between the two data sets. CX13 and CX19 show the largest flux change by a factor of ∼5. We extracted the light curve (0.3–7.0 keV) of CX1, with a time resolution of 2000 s for both data sets 3778 and 5241. The Kolmogorov–Smirnov (K-S) test gives a probability of constancy of 0.39 and 0.09 for data set 3778 and 5241, respectively, which suggests that CX1 may be a constant X-ray source. Figure 3 shows the fitted power-law spectrum and the light curves of CX1.

3. OPTICAL OBSERVATIONS

M92 was observed with the *HST* Advanced Camera for Surveys (ACS) on 2004 August 7 (Proposal ID 10120). In

Table 1
Chandra Source Properties

Source	R.A.	Decl.	Net Counts			$f_{0.3-7}$[a]	$f_{0.5-2.5}$[a]	Optical[b]	*ROSAT*
Name	(J2000.0)	(J2000.0)	Soft	Medium	Hard			Counterpart	No.
CX1	17:17:07.142 (0.03)	+43:08:12.95 (0.02)	248.83	115.36	31.89	3.877	2.607	H & C	X8
CX2	17:17:07.296 (0.05)	+43:08:06.95 (0.04)	49.45	60.17	44.59	1.590	0.955	H & C	
CX3	17:17:06.500 (0.08)	+43:08:03.31 (0.05)	15.90	11.00	9.81	0.376	0.247	H & C	
CX4	17:17:06.816 (0.11)	+43:08:49.47 (0.07)	4.71	13.90	4.71	0.228	0.170	H & C	
CX5	17:17:06.911 (0.18)	+43:08:34.88 (0.10)	2.77	6.88	6.77	0.160	0.070	H & C	
CX6	17:17:07.666 (0.26)	+43:08:05.36 (0.09)	1.43	6.14	3.57	0.113	0.079	H & C	
CX7	17:17:10.520 (0.17)	+43:08:24.36 (0.17)	1.37	4.68	4.68	0.107	0.069	H & C	
CX8	17:17:09.191 (0.17)	+43:08:09.71 (0.14)	4.00	4.00	0.00	0.082	0.066	H & C	
CX9	17:17:08.016 (0.16)	+43:07:59.95 (0.13)	3.90	3.00	0.00	0.072	0.032	H & C	
CX10	17:17:08.089 (0.14)	+43:07:53.94 (0.19)	2.00	1.95	0.95	0.048	0.033	H & C	
CX11	17:17:01.274 (0.05)	+43:10:42.31 (0.02)	216.19	223.54	115.85	5.532	3.543	H	X6
CX12	17:16:35.294 (0.41)	+43:10:31.48 (0.26)	23.59	19.59	8.97	3.224	0.334		
CX13	17:16:54.170 (0.13)	+43:12:01.27 (0.06)	151.06	100.30	10.68	2.673	1.964		
CX14	17:17:12.653 (0.18)	+43:12:51.16 (0.11)	58.17	63.17	20.47	2.398	0.887		
CX15	17:17:22.659 (0.26)	+43:10:55.23 (0.17)	0.00	15.55	29.94	2.315	0.159		
CX16	17:16:46.260 (0.19)	+43:11:17.04 (0.09)	2.60	24.26	132.94	1.839	0.407		
CX17	17:17:10.227 (0.06)	+43:09:45.51 (0.04)	22.71	51.71	31.86	1.052	0.666		
CX18	17:16:38.263 (0.51)	+43:12:14.67 (0.42)	23.73	11.84	2.07	0.934	0.284	V798 Her	XE
CX19	17:17:16.736 (0.52)	+43:12:34.76 (0.23)	8.15	15.65	7.14	0.887	0.172		
CX20	17:16:52.180 (0.49)	+43:12:55.60 (0.27)	13.36	15.07	10.87	0.409	0.263	C	
CX21	17:17:03.249 (0.11)	+43:09:11.12 (0.06)	25.88	11.00	4.00	0.399	0.321	H	
CX22	17:17:23.177 (0.11)	+43:08:16.76 (0.10)	0.84	10.00	11.84	0.312	0.107		
CX23	17:17:06.679 (0.13)	+43:05:46.24 (0.16)	2.33	8.00	11.60	0.296	0.122	C	
CX24	17:16:56.717 (0.13)	+43:07:20.90 (0.09)	6.00	12.84	6.00	0.263	0.172		
CX25	17:16:46.358 (0.48)	+43:07:58.03 (0.17)	5.48	6.74	0.22	0.258	0.094		
CX26	17:17:00.361 (0.42)	+43:13:30.72 (0.30)	6.47	10.28	5.75	0.288	0.133		
CX27	17:17:15.735 (0.16)	+43:10:16.47 (0.11)	0.00	5.00	14.66	0.225	0.062		
CX28	17:17:12.518 (0.53)	+43:13:52.74 (0.43)	0.00	0.92	10.14	0.224	0.022		
CX29	17:16:49.296 (0.24)	+43:08:00.06 (0.16)	0.37	2.79	9.58	0.182	0.36		
CX30	17:16:58.187 (0.17)	+43:06:06.16 (0.13)	7.00	8.00	1.40	0.180	0.124		
CX31	17:16:56.813 (0.19)	+43:05:36.66 (0.20)	7.84	2.67	0.34	0.131	0.088		
CX32	17:16:57.795 (0.15)	+43:07:55.69 (0.14)	6.00	4.88	0.24	0.107	0.090	H	
CX33	17:17:02.143 (0.14)	+43:06:12.02 (0.15)	5.71	3.00	0.31	0.084	0.072		
CX34	17:16:55.054 (0.30)	+43:04:57.07 (0.20)	0.00	0.00	8.74	0.062	0.000		
CX35	17:17:05.365 (0.16)	+43:06:09.95 (0.15)	2.67	3.00	0.67	0.062	0.037	C	
CX36	17:17:25.247 (0.38)	+43:10:19.62 (0.33)	1.56	3.85	1.70	0.598	0.039		
CX37	17:17:11.881 (0.23)	+43:10:33.30 (0.11)	2.00	3.00	0.26	0.052	0.041		
CX38	17:16:55.777 (0.17)	+43:07:09.62 (0.12)	2.00	0.00	2.00	0.045	0.017		
CX39	17:17:15.023 (0.28)	+43:08:32.43 (0.11)	0.93	0.00	3.00	0.040	0.000		

Notes. We have performed astrometry correction for the positions determined by `wavdetect` listed in Table 1. The R.A. and decl. was corrected by $-0\farcs05$ and $-0\farcs09$ respectively and then corrected by the boresight correction (see Section 3.3). The position uncertainties are given by `wavdetect` and in units of arcseconds. Units of right ascension are hours, minutes, and seconds, and units of declination are degrees, arcminutes, and arcseconds (J2000.0). The unabsorbed flux is derived assuming a power-law model with $N_{\rm H} = 1.06 \times 10^{20}$ cm^{-2} and a photon index of 2. The sources listed in the upper part are those inside $r_{\rm h}$ and the lower ones are outside $r_{\rm h}$ of M92. For the *ROSAT* sources see Verbunt (2001); for V798 Her see Geffert (1998).
[a] Unabsorbed flux in units of 10^{-14} erg cm^{-2} s^{-1}.
[b] H: *HST* counterparts; C: CFHT counterparts.

Table 2
Spectral Fits of the Brightest Sources

Source	Model[a]	$N_{\rm H}$[b]	kT/α	χ^2_ν/dof	$f_{0.3-7}$[c]
CX1	TB	5.0	0.7 ± 0.2	1.46/18	2.85
	PL	17.2 ± 8.7	3.8 ± 0.6	1.35/18	2.65
	TB+PL	30.3 ± 15.0	$kT = 0.2 \pm 0.1/\alpha = 0.2 \pm 2.6$	0.91/16	7.01
CX11	PL	6.8	1.8 ± 0.2	0.60/128	6.56
CX13	APEC+PL	21.8	$kT = 0.9 \pm 0.1/\alpha = 2.4 \pm 0.8$	0.92/8	3.31

Notes. All quoted uncertainties are 1σ.
[a] TB: thermal bremsstrahlung; PL: power law.
[b] In units of 10^{20} cm^{-2}. If no error is given, the value indicates an upper limit.
[c] 0.3–7 keV unabsorbed flux in units of 10^{-14} erg cm^{-2} s^{-1}.

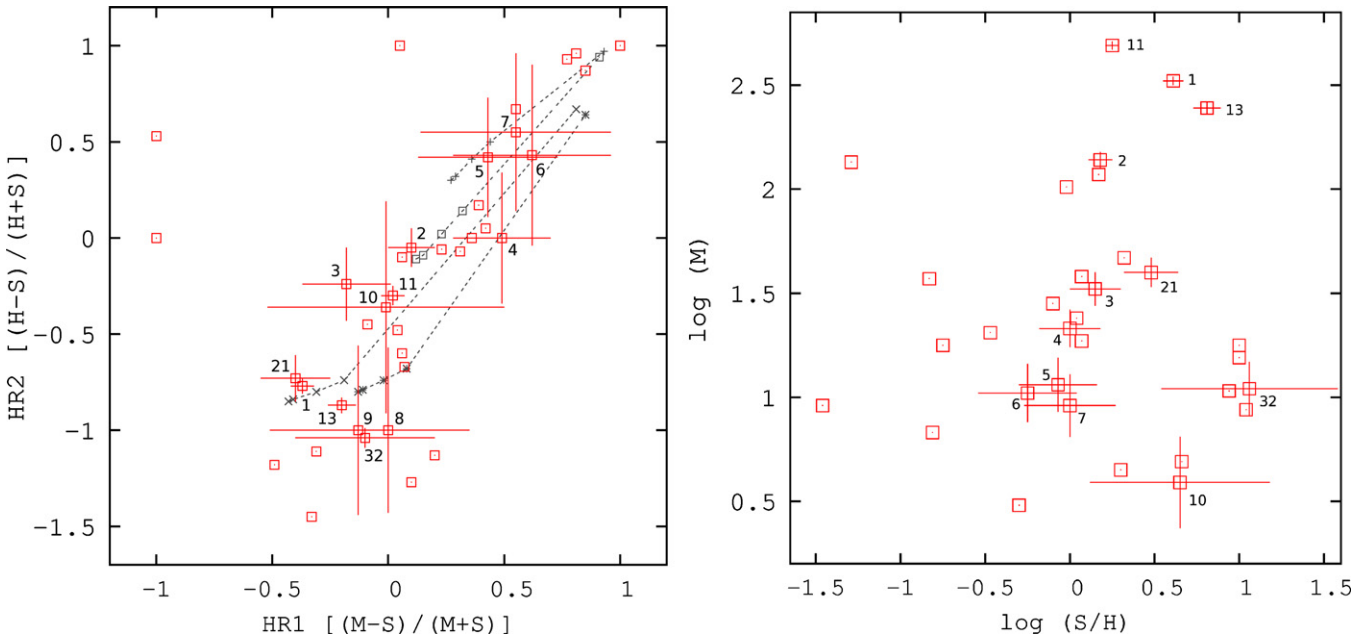

Figure 2. Left: the color–color diagram of the X-ray sources in M92. Numbers indicate sources within r_h. The lines are the hardness ratios predicted from thermal bremsstrahlung (TB) and power-law (PL) model spectra with different column densities, each for a range of column densities. From top to bottom are PL with a photon index of 1, TB with temperature 10 keV, PL with a photon index of 3, and TB with temperature 1 keV. The column densities from left to right are 1×10^{19}, 1.06×10^{20}, 5×10^{20}, 1×10^{21}, and 1×10^{22} cm^{-2}. Right: the color–magnitude diagram of the X-ray sources in M92. The X-ray color is defined as the logarithm of the ratio of 0.5–1.5 keV (S) counts to 1.5–6 keV (H) counts, and the magnitude is the logarithm of 0.5–4.5 keV (M) counts. Sources inside r_h are marked with error bars. CX8 and CX9 are not seen in this diagram since they have zero count in the hard band (1.5–6 keV).

(A color version of this figure is available in the online journal.)

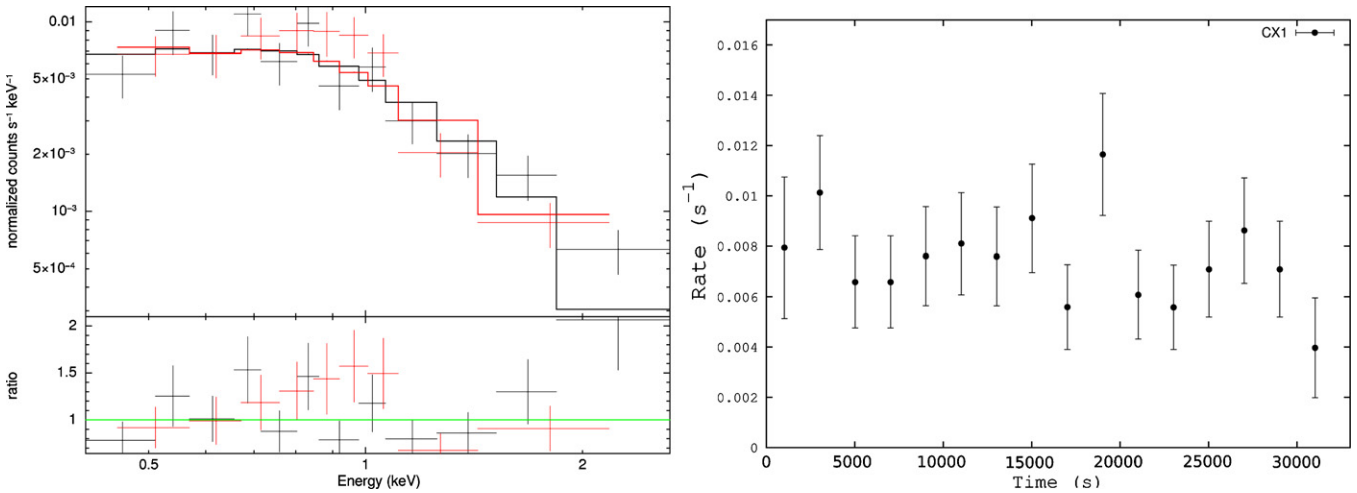

Figure 3. Left: the spectrum of the brightest source (CX1) within the core radius r_c of M92. Black crosses represent the data points from observation 3778 and the red ones from observation 5241. The solid line is the fitted absorbed power law plus thermal bremsstrahlung model. The lower panel is the ratio. The fitted photon index and temperature are 0.18 ± 2.56 and 0.20 ± 0.08 keV. The null hypothesis probability = 56%. Right: the light curve of data set 3778 of CX1 in the energy range 0.3–7.0 keV. Each bin is 2000 s. The total exposure time is ∼29.6 ks. The time zero refers to the instrument time 1.81775×10^8 s. The probability of constancy tested by a Kolmogorov–Smirnov (K-S) test is 39%.

(A color version of this figure is available in the online journal.)

the observation, three filters were used: F435W (B_{435}), F625W (R_{625}), and F658W (Hα_{658}). The exposure time for F435W, F625W, and F658W is 770 s, 370 s, and 1810 s, respectively. The FOV of ACS covers the whole region within r_c and most of the area within r_h. There are 14 X-ray sources within the ACS FOV, of which four are outside r_h (Figure 1).

3.1. Data Reduction

We used individual images for photometry and the ACS drizzled images for astrometry and for identifying the optical counterparts of the X-ray sources. The drizzled images are combined images which have been calibrated for bias, dark current, and flat field. The geometric distortion and cosmic rays are also removed. The calibrations were performed by the ACS calibration pipeline with the tool PyDrizzle.[9]

3.2. Photometry

For photometry, we used individual images and processed them with the package DOLPHOT, a PSF photometry tool

[9] See the *HST* ACS Data Handbook at http://www.stsci.edu/hst/acs/

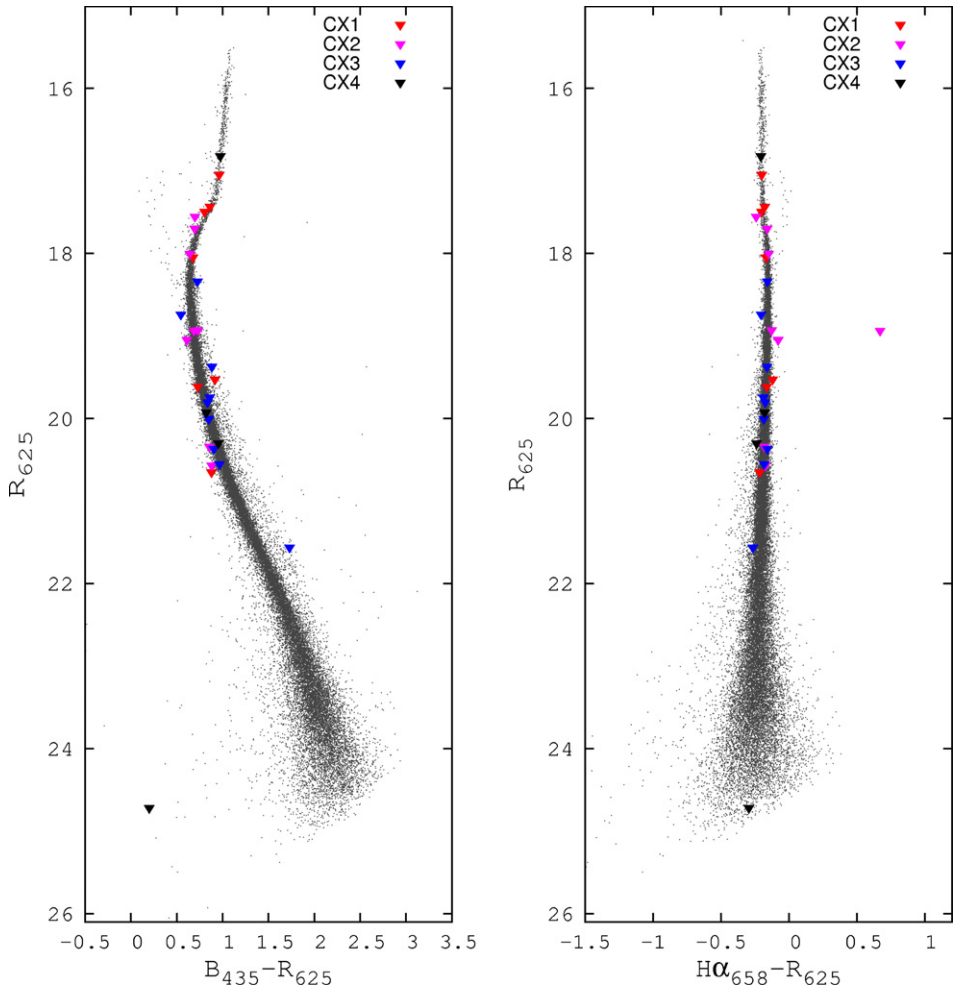

Figure 4. Color–magnitude diagrams (CMDs) of *HST* ACS observation of CX1, CX2, CX3, and CX4 in M92.
(A color version of this figure is available in the online journal.)

adapted from *HSTphot* (Dolphin 2000).[10] DOLPHOT can process multiple images at the same FOV for one run and provide the results of combined photometry for each filter. We applied the DOLPHOT with ACS module in our analysis. First, we run the `acsmask` command on the data quality images provided by the Space Telescope Science Institute in order to mask bad pixels. Then we created a sky map by applying the `calcsky` command. We finally performed `dolphot` to detect sources with ACS PSF and Pixel Area Maps provided by the DOLPHOT ACS module. After the source detection, a master photometry list was produced containing the position, magnitude for each band, signal-to-noise ratio, and other indicators for the detected stars. We set criteria to exclude the cosmic rays, artifacts, and the fake stars located on the diffraction spikes of the saturated stars. Eventually we filtered the output stars and obtained a "good" star list. Stars were selected if they appeared in all three bands. Then we produced the CMDs with the "good" star list (see Figures 4–7).

3.3. Astrometry

The purpose of applying astrometry is to find the correct boresight between the *Chandra* and *HST* images. We therefore performed relative astrometry by individually aligning the *HST* and *Chandra* images on the same reference image frame and coordinate system. The reference image is taken from a wide field optical image. As the reference image, we use an *R*-band archival image of M92 taken with the Canada–France–Hawaii Telescope (CFHT) on 2004 June 10 with a total exposure time of 1250 s, and reprocessed by MegaPipe[11] on 2008 October 7. The MegaPipe reprocessing consists of photometric calibrations (including absolute astrometry) and stacking multiple MegaCam images into one single image. The resultant CFHT image has an FOV of 1° by 1° and M92 is located on the center region, but we only focus on the central 15′ by 15′ area for the following astrometric matching processes.

Since the CFHT MegaCam image had been calibrated for astrometry on the absolute International Celestial Reference System frame, we first aligned *HST* ACS drizzled F625W image onto it. We chose 264 stars on the *HST* image for the matching and fitted them with a six-parameter transformation. The resultant residual error of the transformation solution was 0.″185 in R.A. and 0.″193 in decl.

Before merging the two *Chandra* data sets, we improved the absolute astrometry with the Aspect Calculator,[12] provided by the CXC, on data set 3778 and 5241 individually. The calculator provides an absolute astrometry error of 0.″6 (90%). The calculated offset is 0.″03 in R.A. and −0.″09 in decl. for data

[10] See http://purcell.as.arizona.edu/dolphot/.

[11] MegaPipe is the CFHT MegaCam image stacking pipeline. See http://cadcwww.dao.nrc.ca/megapipe

[12] See http://cxc.harvard.edu/ciao3.4/threads/arcsec_correction/

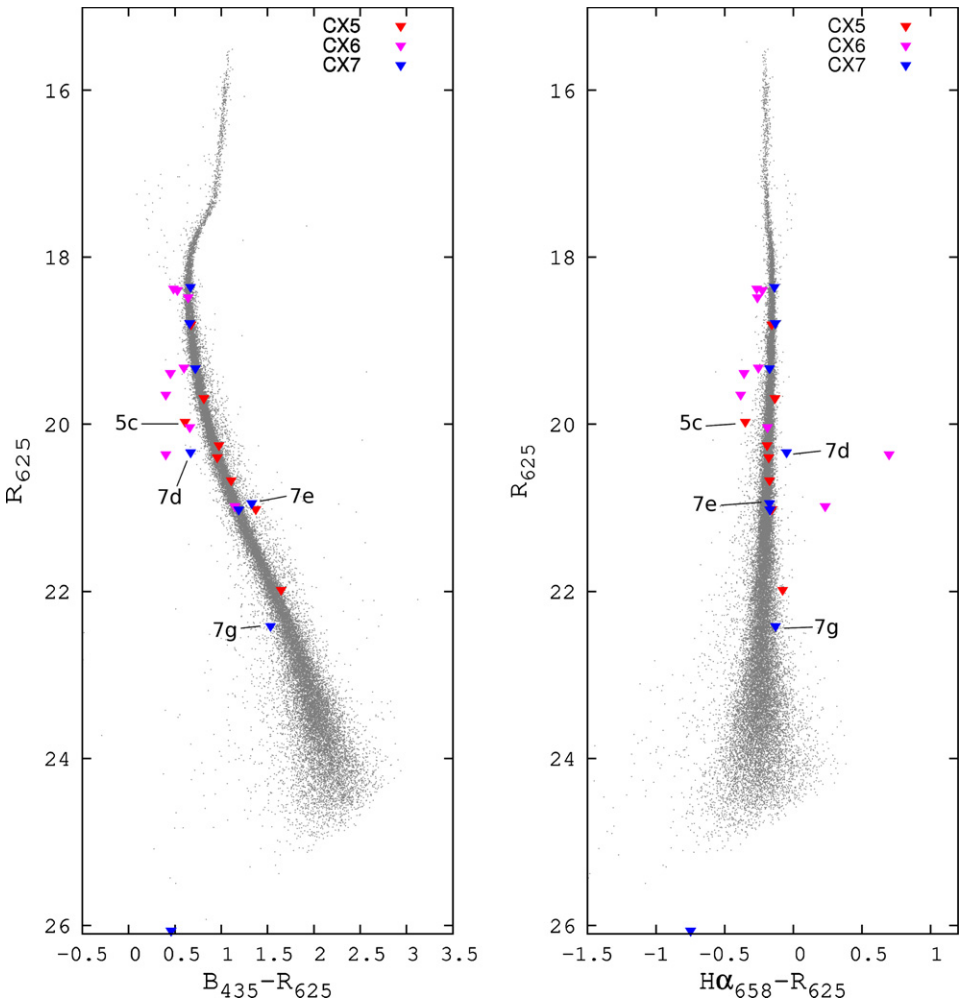

Figure 5. Color–magnitude diagrams (CMDs) of *HST* ACS observation of CX5, CX6, and CX7 in M92.
(A color version of this figure is available in the online journal.)

set 3778 and 0.″05 in R.A. and −0.″09 in decl. for data set 5241. We overlaid the *Chandra* 99% confidence error circles on the CFHT MegaCam image to search for the possible counterparts for star matching. Since the field of the center region of M92 in the MegaCam image is too crowded and most stars inside are saturated, we only considered the stars outside r_h of M92 for astrometry. There are 29 *Chandra* sources outside r_h of M92, with 22 of them having possible MegaCam optical counterparts. However, we did not consider those X-ray sources with multiple CFHT counterparts (except those with central source shaped like a galaxy) to avoid false matches. Furthermore, we did not consider counterparts that are saturated or affected by a nearby saturated star because their imperfect PSF may cause larger positional uncertainties for astrometry. For the X-ray sources with single matches, we did not consider those with faint (and poor PSF) counterparts, either. As a result, we chose the MegaCam optical counterparts of CX20, CX23, and CX35 as our astrometric references to perform boresight correction on the *Chandra* image. The position offset that needs to be applied to the *Chandra* sources is −0.″024 ± 0.″038 in R.A. and −0.″148 ± 0.″020 in decl. After the boresight correction, the MegaCam image and the *Chandra* image are on the same frame.

We accordingly calculated the final uncertainties of the X-ray source position in R.A. and in decl. with the X-ray and optical relative astrometry. The final uncertainties are the root of the quadratic sum of the position uncertainty of the X-ray sources (given in Table 1), the uncertainty of the astrometry in the MegaCam and *HST* image alignment, and the uncertainty of the X-ray boresight correction. We note that the position uncertainty of the X-ray sources includes the errors resulted from the image distortion at the edge of *Chandra* CCD. The final 1σ position error for all X-ray sources varies from $\sim$ 0.″3 to 0.″7. We took all the *HST* sources inside the 95% ($\sim$2.48σ) confidence X-ray error circle as the possible counterparts in the optical band. The 5″ × 5″ finding charts of the 10 sources within r_h are listed in Figure 8.

An independent check on our astrometry can be made from the identification of CX18 with V798 Her. The position for V798 Her as given in the astrometric study by Tucholke et al. (1996) agrees within the error to the position of CX18 in Table 1.

4. SOURCE IDENTIFICATION AND CLASSIFICATION

In Figure 8 we show the optical images for the regions near the X-ray sources within the FOV of our *HST* observations, together with the 95% error areas. It is seen that each error area within the core of M92 contains more than one optical object, often many more. Thus, most optical objects are in the error boxes by chance, and we cannot assign optical counterparts to the core sources on the basis of positional coincidence only.

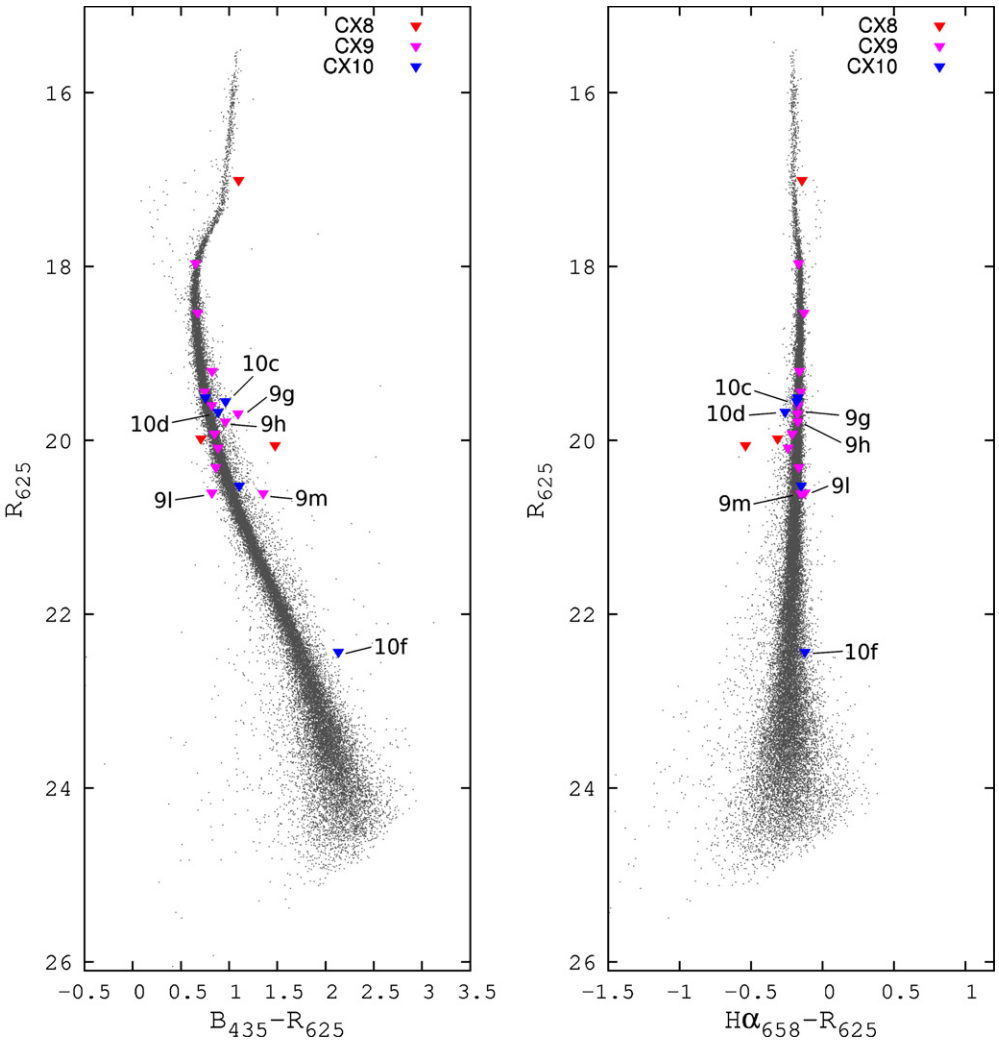

Figure 6. Color–magnitude diagrams (CMDs) of *HST* ACS observation of CX8, CX9, and CX10 in M92.
(A color version of this figure is available in the online journal.)

Optical counterparts of LMXBs and CVs are often blue, and often have Hα in emission. ABs may lie above the main sequence, if both stars contribute significantly to the total light. To investigate the optical sources further, we therefore indicate all *HST* optical sources within the 95% error circles of the *Chandra* sources in the CMD of M92, in Figures 4–7. The magnitudes of these sources are listed with some additional information in Table 3, where the candidate counterparts for each source are ordered on the *R* magnitude, and denoted by a, b, etc., accordingly.

We further make use of the relation between the highest X-ray luminosity and the bolometric luminosity for ABs,

$$L_x < 0.001\, L_{\rm bol}. \quad (1)$$

Using the relation between bolometric luminosity and absolute visual magnitude for main-sequence stars, this may be converted to a relation between the maximum L_x and M_V: this relation is shown in Figures 9 and 10 (see Bassa et al. 2008). The maximum 0.5–2.5 keV luminosity for ABs with main-sequence components is about 10^{31} erg s^{-1}. This relation may be compared with an empirical separation between CVs and ABs, derived from early observations of these sources in GCs (Bassa et al. 2004):

$$\log L_{0.5-2.5\,\rm keV} = 34.0 - 0.4\, M_V. \quad (2)$$

We note that our CV samples from early observations are those with main-sequence companions. These lines are shown in Figures 9 and 10, together with data from earlier papers of 47 Tuc, NGC 6752, M4, and NGC 288 (Grindlay et al. 2001; Pooley et al. 2002b; Bassa et al. 2004; Kong et al. 2006), and the candidate counterparts for M92. The sources between these lines are puzzling: they were classified as ABs in early papers because their optical colors are those of main-sequence stars, but they have higher X-ray luminosities than ABs of the same absolute visual magnitude near the Sun (Verbunt et al. 2007).

One can also use the X-ray colors (Figure 2) in classifying the X-ray sources; only the brightest sources, or the extreme cases, have enough counts to produce a significant discriminant.

4.1. Sources Inside the Half-mass Radius

If we assume that any of the optical objects in the error boxes of the three brightest X-ray sources, CX1 (*ROSAT* source X8), CX2, and CX3, is the counterpart of the X-ray source, the resulting X-ray-to-optical luminosity would be higher than the maximum ratio for an AB, given by Equation (2), as shown in Figure 9. This indicates that these three sources are not ABs. They may be members of the class of puzzling sources, located in Figure 9 between the relations defined by Equations (1) and (2), but their X-ray luminosities are high compared with those

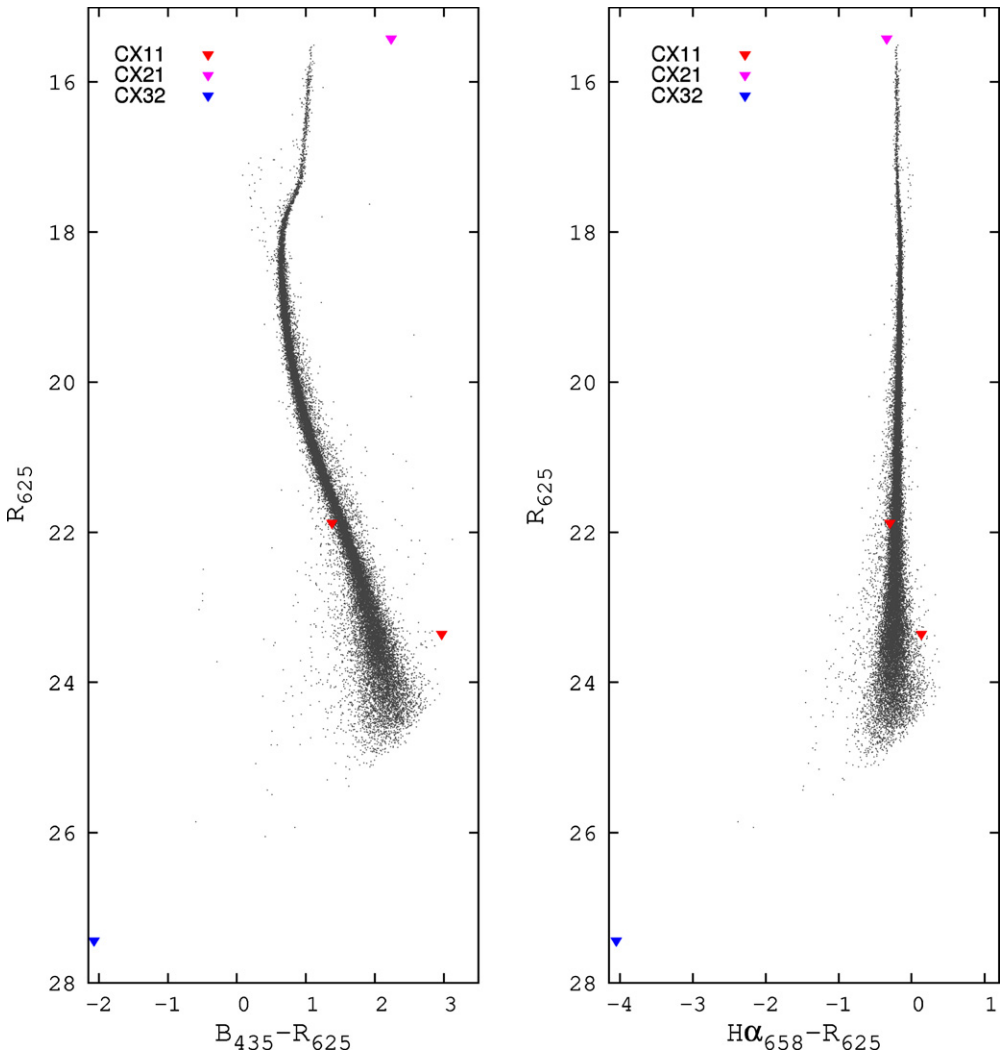

Figure 7. Color–magnitude diagrams (CMDs) of *HST* ACS observation of CX11, CX21, and CX32 in M92.
(A color version of this figure is available in the online journal.)

of such objects found in earlier studies, and we consider it more likely that they are CVs. The luminosity of CX1 (*ROSAT* source X8) suggests that it may be an LMXB, particularly if we take into account its higher luminosity level in 1992 August (see the Introduction). However, the optical colors of the optical objects are not those expected for CVs, i.e., they are not significantly bluer than the main sequence and do not show Hα in emission. It appears then, that we have not detected the optical counterpart of these X-ray sources, and that the actual counterpart is fainter.

A similar reasoning holds for all but the brightest and faintest optical stars in the error circle of CX4. The brightest star is a giant, the faintest is blue. Perhaps the latter is the most likely counterpart, in which case it may well be a background galaxy (Figure 9).

Most of the optical objects in the error boxes of CX5–CX10 would, when accepted as the counterpart of the X-ray source, be located in Figure 9 between the relations defined by Equations (1) and (2), in an area where similar sources were found in earlier studies of other GCs. We briefly consider some optical objects that are not on the main sequence in the CMDs of Figures 5 and 6 (see Table 3). CX5c is to the blue of the main sequence and has Hα in emission; this makes it the probable counterpart of CX5 and a CV. The optical objects in the error circle of CX6 are almost all away from the main sequence; this suggests that their colors are affected by the nearby bright star (see Figure 8). It is not clear which if any of these optical objects is the counterpart to CX6. CX7d and CX7g are to the blue of the main sequence, but have Hα in absorption. If either of these is the counterpart, the source may be a CV (though having Hα strongly in absorption would then be somewhat surprising). CX7e is above the main sequence and if it is the counterpart would be above the relation given by Equation (2). CX8a is saturated in the optical bands; if it is the counterpart of the relatively soft X-ray source CX8, it may be a foreground star. None of the other three stars are on the main sequence, suggesting that their photometry is contaminated by CX8a. CX9a is saturated in the optical bands; if it is the counterpart of the relatively soft X-ray source CX9, it may be a foreground star. CX9l is to the blue of the main sequence, and if the counterpart may be a CV, CX9g, CX9m, and to a lesser extent CX9h are above the main sequence; each of these could be the counterpart to the X-ray source, which then is an AB. Finally, CX10a is also saturated. Of the other stars in the error box CX10d has Hα emission, its $B - R$ is on the main sequence. CX10c and CX10f are above the main sequence.

Table 3
Optical Counterparts to *Chandra* X-Ray Sources

Source[a] Name	Δ R.A. (arcsec)	Δ Decl. (arcsec)	B_{435}	R_{625}[b]	Hα_{658}	$L_{X(0.3-7)}$[c]	M_V[d]	f_X/f_r[e]	Classification[f]
1a	0.33	−0.08	18.010 ± 0.004	17.048 ± 0.002	16.847 ± 0.002	3.12E+32	2.89	0.056	CC
1b	−0.15	0.35	18.297 ± 0.001	17.435 ± 0.001	17.257 ± 0.003		3.23	0.080	CC
1c	0.10	0.22	18.299 ± 0.001	17.497 ± 0.001	17.295 ± 0.002		3.26	0.085	CC
1d	0.25	−0.31	18.725 ± 0.002	18.050 ± 0.002	17.882 ± 0.004		3.75	0.141	CC
1e	0.09	0.00	20.443 ± 0.005	19.528 ± 0.005	19.407 ± 0.009		5.35	0.551	CV?
1f	−0.04	−0.06	20.342 ± 0.004	19.615 ± 0.005	19.452 ± 0.009		5.34	0.597	CC
1g	−0.06	0.14	21.530 ± 0.010	20.652 ± 0.009	20.436 ± 0.018		6.45	1.522	CV
2a	0.02	0.30	18.252 ± 0.001	17.555 ± 0.002	17.314 ± 0.003	1.28E+32	3.26	0.033	CC
2b	0.06	0.12	18.396 ± 0.002	17.700 ± 0.002	17.539 ± 0.003		3.41	0.037	CC
2c	0.21	−0.24	18.645 ± 0.002	18.003 ± 0.002	17.853 ± 0.004		3.68	0.049	CC
2d	0.09	−0.03	19.661 ± 0.003	18.931 ± 0.003	18.802 ± 0.007		4.66	0.116	CC
2e	0.04	0.42	19.621 ± 0.005	18.936 ± 0.006	19.606 ± 0.014		4.64	0.116	CC
2f	−0.21	0.14	19.658 ± 0.003	19.048 ± 0.003	18.968 ± 0.006		4.71	0.129	CV
2g	0.36	0.11	21.196 ± 0.008	20.341 ± 0.008	20.159 ± 0.015		6.13	0.424	CC
2h	0.28	−0.05	21.447 ± 0.009	20.568 ± 0.009	20.394 ± 0.018		6.37	0.523	CV?
3a	−0.15	0.26	19.066 ± 0.002	18.341 ± 0.003	18.182 ± 0.005	3.03E+31	4.06	0.016	CC
3b	−0.04	0.25	19.284 ± 0.002	18.741 ± 0.003	18.536 ± 0.005		4.37	0.024	CV
3c	0.20	−0.11	20.255 ± 0.004	19.373 ± 0.004	19.211 ± 0.007		5.17	0.042	CC
3d	−0.18	0.10	20.604 ± 0.005	19.745 ± 0.005	19.556 ± 0.009		5.54	0.060	CC
3e	−0.37	−0.28	20.639 ± 0.005	19.804 ± 0.005	19.629 ± 0.010		5.58	0.063	CC
3f	−0.12	−0.23	20.853 ± 0.005	20.005 ± 0.005	19.819 ± 0.010		5.79	0.076	CC
3g	−0.31	−0.34	21.272 ± 0.008	20.369 ± 0.008	20.210 ± 0.017		6.18	0.106	CC
3h	0.37	−0.28	21.519 ± 0.008	20.553 ± 0.007	20.370 ± 0.014		6.40	0.126	CC
3i	−0.36	−0.09	23.292 ± 0.030	21.563 ± 0.016	21.297 ± 0.028		7.79	0.319	CC
4a	−0.18	−0.23	17.796 ± 0.003	16.822 ± 0.007	16.615 ± 0.002	1.83E+31	2.67	0.003	AB?
4b	−0.41	0.04	20.748 ± 0.005	19.927 ± 0.005	19.748 ± 0.009		5.70	0.048	CC
4c	0.02	0.19	21.253 ± 0.006	20.299 ± 0.006	20.060 ± 0.011		6.14	0.068	CV?
4d	0.16	−0.47	24.918 ± 0.070	24.719 ± 0.146	24.424 ± 0.271		10.15	3.977	AGN?
5a	−0.11	0.00	19.477 ± 0.002	18.804 ± 0.003	18.647 ± 0.005	1.29E+31	4.50	0.008	CC
5b	0.21	0.24	20.501 ± 0.004	19.690 ± 0.004	19.556 ± 0.009		5.46	0.018	CC
5c	−0.14	0.15	20.580 ± 0.005	19.972 ± 0.005	19.622 ± 0.009		5.64	0.023	CV
5d	−0.01	0.03	21.226 ± 0.006	20.252 ± 0.006	20.060 ± 0.011		6.10	0.030	CC
5e	0.19	0.01	21.355 ± 0.007	20.398 ± 0.007	20.219 ± 0.013		6.24	0.035	CC
5f	0.20	−0.06	21.781 ± 0.008	20.674 ± 0.007	20.501 ± 0.015		6.59	0.045	CC
5g	0.39	0.31	22.391 ± 0.014	21.019 ± 0.010	20.862 ± 0.021		7.07	0.061	CV?
5h	−0.20	−0.45	23.625 ± 0.025	21.979 ± 0.016	21.901 ± 0.035		8.16	0.148	CV?
6b	−0.23	−0.04	18.860 ± 0.002	18.376 ± 0.003	18.109 ± 0.005	9.11E+30	3.98	0.005	AB?
6c	−0.27	0.21	18.919 ± 0.002	18.393 ± 0.003	18.167 ± 0.005		4.02	0.005	AB?
6d	0.23	−0.36	19.124 ± 0.002	18.482 ± 0.003	18.220 ± 0.005		4.16	0.006	AB?
6e	−0.03	0.30	19.920 ± 0.004	19.324 ± 0.004	19.069 ± 0.008		4.98	0.012	CV?
6f	−0.13	0.12	19.841 ± 0.004	19.390 ± 0.006	19.031 ± 0.008		4.98	0.013	CV?
6g	0.19	−0.16	20.046 ± 0.004	19.646 ± 0.007	19.262 ± 0.010		5.21	0.016	CV?
6h	−0.64	0.24	20.698 ± 0.009	20.038 ± 0.011	19.849 ± 0.019		5.73	0.023	CV?
6i	−0.41	0.19	20.763 ± 0.010	20.363 ± 0.014	21.061 ± 0.027		5.92	0.032	CC
6j	0.33	0.23	22.130 ± 0.026	20.984 ± 0.022	21.216 ± 0.038		6.92	0.056	CC
7a	−0.29	0.39	19.022 ± 0.002	18.355 ± 0.002	18.217 ± 0.004	8.61E+30	4.05	0.004	CC
7b	0.05	−0.32	19.449 ± 0.003	18.791 ± 0.003	18.659 ± 0.006		4.48	0.006	CC
7c	0.11	−0.21	20.051 ± 0.004	19.331 ± 0.004	19.158 ± 0.008		5.05	0.010	CC
7d	0.04	−0.04	21.007 ± 0.019	20.338 ± 0.022	20.289 ± 0.049		6.03	0.025	CV?
7e	−0.58	−0.07	22.276 ± 0.010	20.948 ± 0.008	20.775 ± 0.016		6.97	0.043	CC
7f	−0.54	0.12	22.213 ± 0.010	21.024 ± 0.008	20.854 ± 0.018		6.98	0.046	CC
7g	0.43	−0.17	23.945 ± 0.030	22.413 ± 0.019	22.283 ± 0.042		8.54	0.166	CV?
7h	−0.38	0.26	26.521 ± 0.441	26.063 ± 0.435	25.314 ± 0.718		11.65	4.789	AGN?
8b	−0.07	0.11	18.106 ± 0.001	17.008 ± 0.008	16.864 ± 0.002	6.59E+30	2.92	0.001	CC
8c	−0.28	0.50	20.685 ± 0.006	19.978 ± 0.006	19.663 ± 0.010		5.69	0.023	CV?
8d	−0.11	0.35	21.534 ± 0.010	20.058 ± 0.007	19.519 ± 0.010		6.16	0.025	CC
9b	0.39	−0.39	18.616 ± 0.002	17.964 ± 0.002	17.797 ± 0.004	5.77E+30	3.65	0.002	AB?
9c	−0.32	0.11	19.206 ± 0.007	18.533 ± 0.003	18.403 ± 0.005		4.23	0.003	AB?
9d	0.17	0.18	20.025 ± 0.004	19.203 ± 0.004	19.042 ± 0.007		4.97	0.006	AB?
9e	0.51	0.23	20.182 ± 0.004	19.437 ± 0.004	19.285 ± 0.008		5.17	0.007	AB?
9f	−0.56	0.05	20.416 ± 0.004	19.595 ± 0.005	19.425 ± 0.008		5.37	0.008	AB?
9g	−0.20	−0.42	20.784 ± 0.006	19.692 ± 0.004	19.518 ± 0.009		5.60	0.009	AB?
9h	0.37	−0.05	20.745 ± 0.005	19.784 ± 0.005	19.612 ± 0.009		5.62	0.009	AB?

Table 3
(Continued)

Source[a] Name	Δ R.A. (arcsec)	Δ Decl. (arcsec)	B_{435}	R_{625}[b]	Hα_{658}	$L_{X(0.3-7)}$[c]	M_V[d]	f_X/f_r[e]	Classification[f]
9i	−0.21	0.37	20.771 ± 0.006	19.923 ± 0.005	19.711 ± 0.010		5.71	0.011	AB?
9j	0.20	−0.05	20.970 ± 0.007	20.086 ± 0.007	19.846 ± 0.011		5.89	0.012	AB?
9k	0.08	0.41	21.170 ± 0.007	20.39 ± 0.007	20.143 ± 0.013		6.10	0.015	AB?
9l	−0.55	0.28	21.425 ± 0.008	20.604 ± 0.008	20.479 ± 0.015		6.35	0.020	CV?
9m	0.35	0.39	21.962 ± 0.010	20.609 ± 0.008	20.456 ± 0.015		6.65	0.020	CV?
10b	−0.25	−0.09	20.265 ± 0.004	19.510 ± 0.004	19.337 ± 0.008	3.87E+30	5.25	0.007	CC
10c	−0.12	0.41	20.515 ± 0.005	19.552 ± 0.004	19.372 ± 0.008		5.39	0.007	AB?
10d	−0.12	0.16	20.558 ± 0.005	19.673 ± 0.005	19.411 ± 0.009		5.48	0.008	AB?
10e	−0.27	0.21	21.626 ± 0.008	20.521 ± 0.007	20.372 ± 0.014		6.43	0.018	AB?
10f	−0.44	0.09	24.566 ± 0.060	22.434 ± 0.023	22.311 ± 0.050		8.86	0.103	CV?
11a	−0.11	0.15	23.251 ± 0.015	21.872 ± 0.013	21.576 ± 0.025	4.45E+32	7.92	6.336	CV
11b	0.06	0.15	26.320 ± 0.117	23.351 ± 0.032	23.486 ± 0.095		10.20	24.740	CC
21a	0.13	−0.23	17.659 ± 0.003	15.423 ± 0.003	15.083 ± 0.002	3.21E+31	1.90	0.001	CC
32a	0.12	0.40	25.368 ± 0.075	27.437 ± 9.999	23.385 ± 0.091	8.60E+30	11.76	28.497	AGN

Notes.
[a] The counterparts are ordered with increasing R_{625} band magnitude.
[b] The errors in B_{435} and R_{625} only reflect statistical uncertainty and do not include any systematic errors.
[c] X-ray luminosity derived in the 0.3–7 keV band assuming cluster membership.
[d] Absolute V-band magnitude assuming cluster membership. The apparent V-band magnitude is computed from $(B_{435} + R_{625})/2$.
[e] Ratio of X-ray to optical (R_{625}) flux, using $\log(f_X/f_r) = \log f_X + 5.67 + 0.4R_{625}$ (Green et al. 2004); f_X is derived in the 0.5–2 keV band.
[f] The tentative classifications of multiple sources are valid only if the counterparts are true. CV: cataclysmic variable; AB: chromospherically active binary; CC: chance counterpart (the optical source is located inside the error circle by chance).

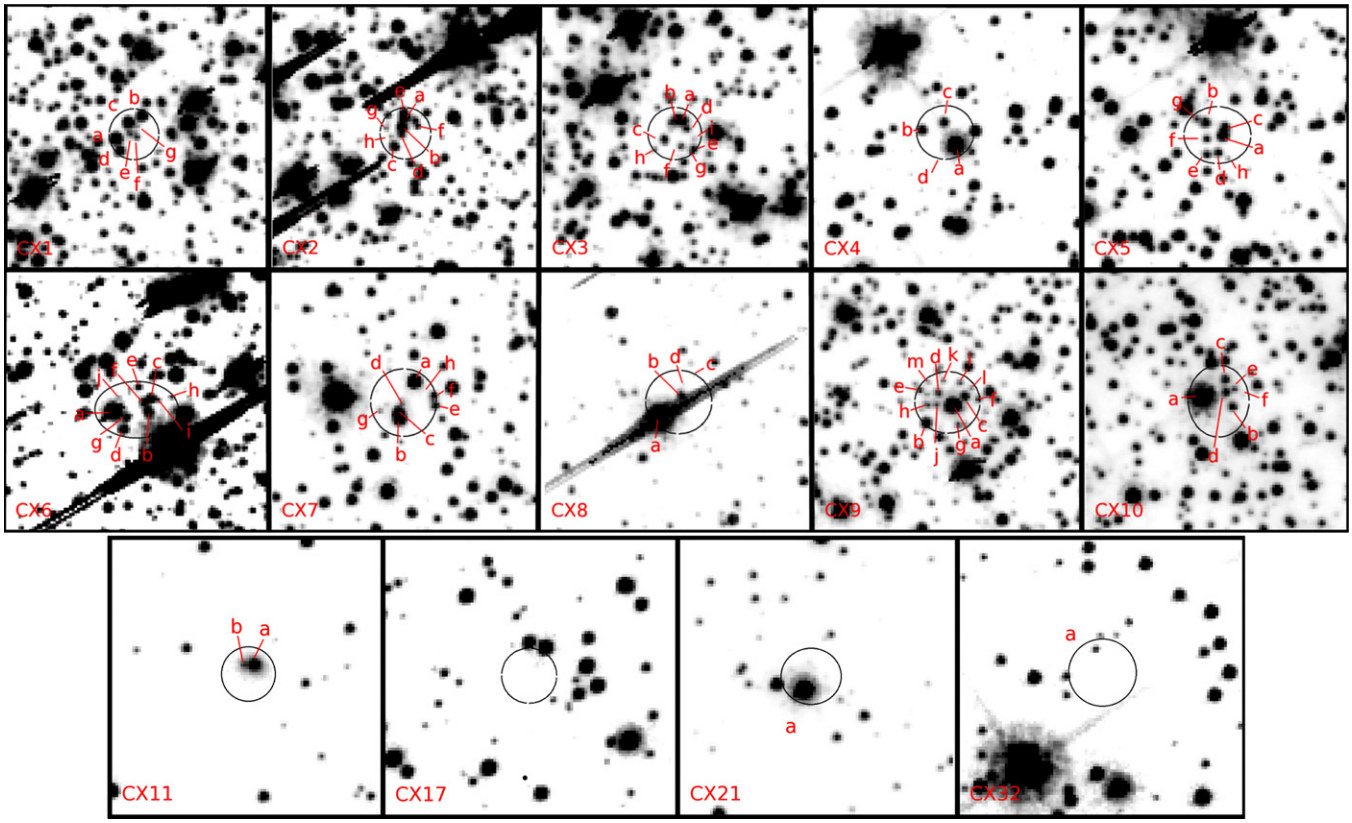

Figure 8. 5″ × 5″ finding charts for the X-ray sources inside the *HST* ACS field of view. The background optical image is the drizzled *R*-band (F625W) *HST* image. The 95% error circles of X-ray sources have been laid on the charts. The optical counterpart candidates are marked with letters. The gray scales of the fourteen images are different in order to show the counterparts clearly. In all the images, north is up and east is left.
(A color version of this figure is available in the online journal.)

In summary, we consider CX1 a probable member of M92, a qLMXB or a bright CV. On the basis of their X-ray luminosities, CX2 and CX3 are probably CVs, and so is CX4 unless it is a background galaxy. CX5 is probably a CV because of its optical

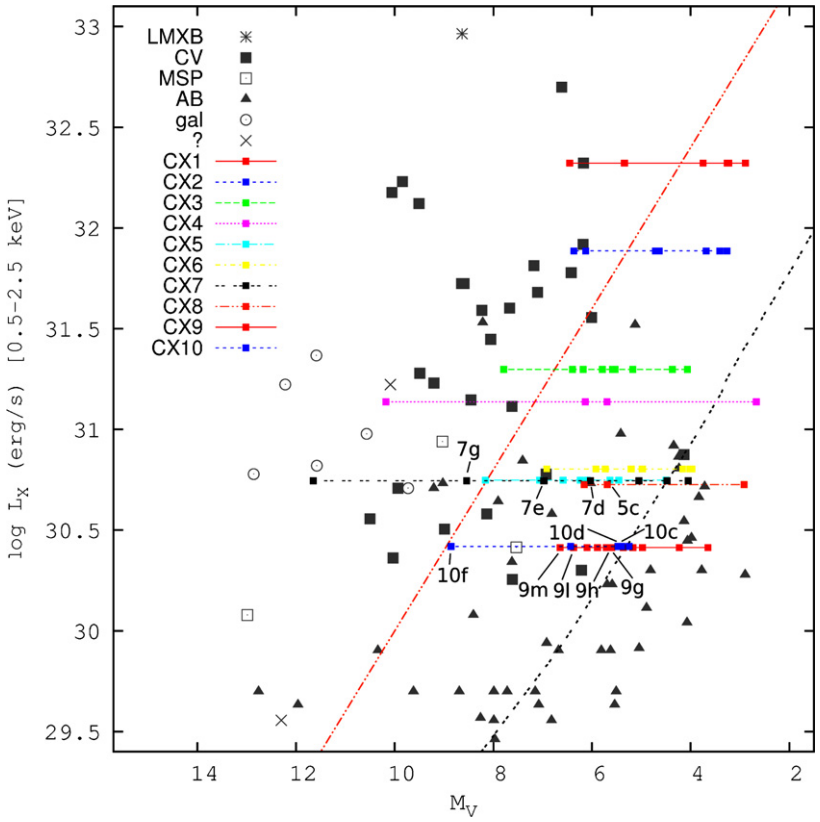

Figure 9. Diagram of the 0.5–2.5 keV X-ray luminosity to the *V*-band absolute magnitude for the 10 sources within r_h. The optical counterparts for each X-ray source are connected with a horizontal line. The *V*-band magnitudes are derived from $V = (B435+r625)/2$. The dashed red line represents the formula $\log L_X = 34.0 - 0.4\,M_V$ (after Bassa et al. 2004) that is the constant X-ray to optical flux ratio roughly separating CVs and ABs. The gray dashed line is computed from 11.2 Gyr isochrones for $z = 0.001$ from Girardi et al. (2000) and represents the maximum X-ray luminosities of ABs in the solar neighborhood and in globular clusters, respectively, assuming $L_X \simeq 0.001\,L_{bol}$. Other data points are the sources identified from 47Tuc, M4, NGC 6752, and NGC 288.

(A color version of this figure is available in the online journal.)

counterpart. The expected number of three background sources within the half-mass radius of M92 must be looked for among the fainter X-ray sources, CX6 to CX10. In the absence of secure counterparts, we cannot say which, if any, of these sources is a member of M92.

4.2. Sources Outside the Half-mass Radius

Four of the sources outside the half-mass radius fall within the FOV of our *HST* observations (Figure 1). The error circles of the X-ray positions on the optical frame are shown in Figure 8. The optical properties of the objects within the error circles are shown in Figure 7, and the comparison of X-ray to optical flux in Figure 10.

CX11 is the brightest X-ray source outside r_h. It corresponds to *ROSAT* source X6, its luminosity in the 0.5–2.5 keV band is the same in the *Chandra* and *ROSAT* observations, within the error. The spectrum of CX11 could be fitted with a power-law model with photon index ∼1.8, a relatively soft X-ray spectrum (Table 2). CX11a has a slightly blue color and Hα emission. The optical properties suggest that it is the real counterpart of CX11, and if associated with M92 that it is a CV.

There is no *HST* optical counterpart for CX17.

The one optical counterpart for CX21 is too far away from the main sequence in the CMD (Figure 7) to be a cluster member. It is very red, with a low X-ray to optical ratio, and thus likely a foreground star.

CX32 is faint in X-ray and has one possible faint optical counterpart. We suggest that it is an AGN, i.e., a background source.

Of the sources outside the FOV of our *HST* observations, we mention CX18: this source corresponds to *ROSAT* source XE and is the W UMa variable V798 Her. This variable is not related to M92. The X-ray flux in the 0.5–2.5 keV band is the same within the error in the *Chandra* and *ROSAT* observations.

5. DISCUSSION

Our *Chandra* observation detected 10 X-ray sources within the half-mass radius of M92. Background estimates suggest that two or three of these are background sources. The brightest source, CX1 (= *ROSAT* X8), is probably still unidentified. It is probably a cluster member, possibly an LMXB in a low state. If it is a CV, it may well be a DQ Her system: among the CVs this class has the highest X-ray luminosities (see, e.g., Figure 8 of Verbunt et al. 1997), and it also often shows internal absorption, in agreement with the finding by Verbunt (2001) and by us that the absorption column to CX1 is higher than expected for a member of M92 (Table 2).

We think that the sources CX2, CX3, and CX5 are also cluster members, based on the X-ray luminosity for CX2 and CX3, and based on the optical counterpart for CX5. CX4 may also be a CV in the cluster, or a background AGN. Of the remaining five sources within the half-mass radius, several and possibly all are background sources.

The relatively high star density within the half-mass radius of M92 and its large distance lead to the presence of multiple candidate optical counterparts in each X-ray error circle, and precludes certain identifications. Only a variability study may

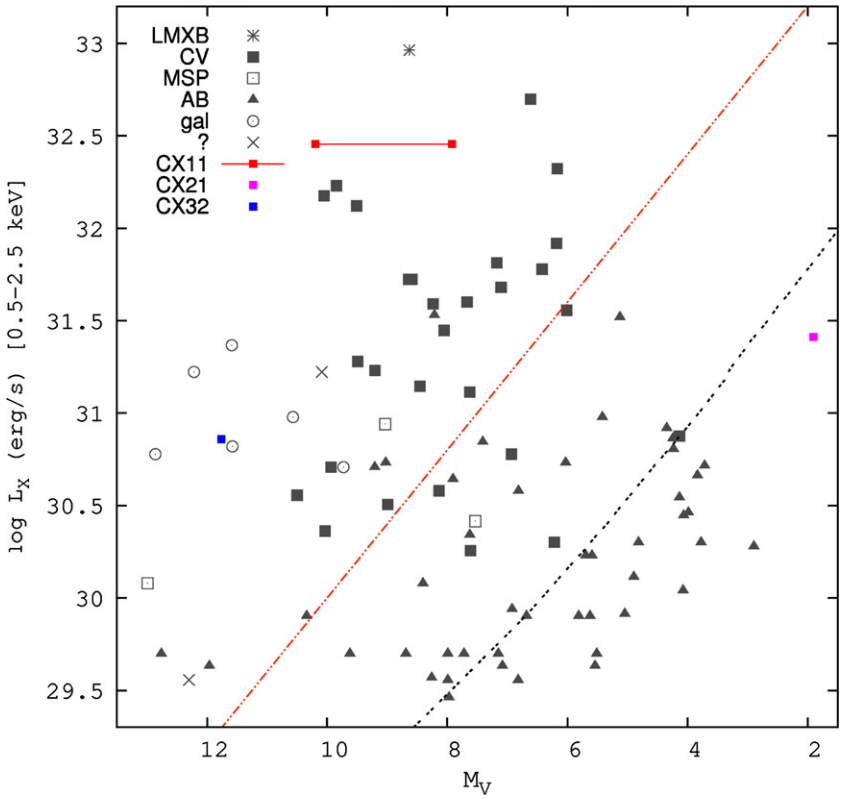

Figure 10. Diagram of the 0.5–2.5 keV X-ray luminosity to the *V*-band absolute magnitude for CX11, CX21, and CX32. See the caption of Figure 9 for the labels description.

(A color version of this figure is available in the online journal.)

be able to identify optical variations characteristic of, e.g., dwarf novae, but here also the crowding of optical sources may hamper progress: it is probable that we have not detected the optical counterpart of any of the four brightest X-ray sources in M92.

The expected number of X-ray sources formed via dynamical encounters scales with the number of encounters in the cluster, which is proportional to the collision number $\Gamma \propto \rho_o^{1.5} r_c^2$, where ρ_o is the central density of the cluster. The expected number of primordial binaries scales with the (half-)mass $(0.5\times)M$ of the cluster. When the mass-to-light ratio for all clusters is the same, the central density scales linearly with the central luminosity, and the mass of the cluster with $10^{-0.4\,M_V}$, where M_V is the absolute visual magnitude. For X-ray sources with $L_{\rm X(0.5-6\,keV)} > 4\times10^{30}$ erg s^{-1}, Pooley & Hut (2006) show that the total number of X-ray sources in a cluster may be expressed as

$$N = a\Gamma + bM. \quad (3)$$

A detailed fit to the results of some 15 clusters gives $a = 1.2$ and $b = 1.1$ when Γ and M are scaled to the values for the globular cluster M4 (Lan et al. 2010; Bassa et al. 2008). Note that the fit by Lan et al. is based on the mass and collision number of M4 derived from the values given by Richer et al. (1997). We use the same normalization, but take the values for central density, core radius, and absolute visual magnitude for M92 from Harris (1996, 2010 version) to predict eight sources formed in M92 via stellar encounters and four formed from primordial binaries, with luminosities above $L_{\rm X(0.5-6\,keV)} > 4\times10^{30}$ erg s^{-1}. Within the statistical errors, these numbers are compatible with our finding of nine such sources within the half-mass radius of M92 with the required X-ray luminosity, of which 1–3 may be background sources. Based on the prediction, the number of primordial X-ray sources in M92 is expected to be significant. We therefore suggest that the X-ray sources in M92 are formed not only through dynamical interactions but through primordial binaries, while at least one X-ray source in M92 is formed primordially.

We thank Andrew Dolphin for providing a modified version of his DOLPHOT code. This project is supported by the National Science Council of the Republic of China (Taiwan) through grant NSC 96-2112-M-007-037-MY3 and NSC 99-2112-M-007-004-MY3. This research is based on observations made with the NASA/ESA *Hubble Space Telescope*, obtained from the Data Archive at the Space Telescope Science Institute, which is operated by the Association of Universities for Research in Astronomy, Inc., under NASA contract NAS 5-26555. These observations are associated with program 10120.

REFERENCES

Bassa, C., et al. 2004, ApJ, 609, 755
Bassa, C. G., Pooley, D., Verbunt, F., Homer, L., Anderson, S. F., & Lewin, W. H. G. 2008, A&A, 488, 921
Becker, W., et al. 2003, ApJ, 594, 798
Brandt, W. N., et al. 2001, AJ, 122, 2810
Clark, G. W. 1975, ApJ, 199, L143
Cohn, H. N., et al. 2010, ApJ, 722, 20
Dolphin, A. E. 2000, PASP, 112, 1383
Edmonds, P. D., Gilliland, R. L., Heinke, C. O., & Grindlay, J. E. 2003, ApJ, 596, 1177
Fabian, A. C., Pringle, J. E., & Rees, M. J. 1975, MNRAS, 172, 15P
Ferraro, F. R., Paltrinieri, B., Rood, R. T., Fusi Pecci, F., & Buonanno, R. 2000, ApJ, 537, 312
Fox, D., Lewin, W., Margon, B., van Paradijs, J., & Verbunt, F. 1996, MNRAS, 282, 1027

Geffert, M. 1998, A&A, 340, 305
Girardi, L., Bressan, A., Bertelli, G., & Chiosi, C. 2000, A&AS, 141, 371
Green, P. J., et al. 2004, ApJS, 150, 43
Grindlay, J. E., Camilo, F., Heinke, C. O., Edmonds, P. D., Cohn, H., & Lugger, P. 2002, ApJ, 581, 470
Grindlay, J. E., Heinke, C., Edmonds, P. D., & Murray, S. S. 2001, Science, 292, 2290
Harris, W. E. 1996, AJ, 112, 1487
Heinke, C. O., Grindlay, J. E., Edmonds, P. D., Cohn, H. N., Lugger, P. M., Camilo, F., Bogdanov, S., & Freire, P. C. 2005, ApJ, 625, 796
Hertz, P., & Grindlay, J. E. 1983, ApJ, 267, L83
Hills, J. G. 1976, MNRAS, 175, 1P
Huang, R. H. H., Becker, W., Edmonds, P. D., Elsner, R. F., Heinke, C. O., & Hsieh, B. C. 2010, A&A, 513, A16
Hurley, J. R., Aarseth, S. J., & Shara, M. M. 2007, ApJ, 665, 707
Hut, P., et al. 1992, PASP, 104, 981
Johnston, H. M., Verbunt, F., & Hasinger, G. 1994, A&A, 289, 763
Katz, J. I. 1975, Nature, 253, 698
Kong, A. K. H., Bassa, C., Pooley, D., Lewin, W. H. G., Homer, L., Verbunt, F., Anderson, S. F., & Margon, B. 2006, ApJ, 647, 1065
Kopacki, G. 2001, A&A, 369, 862
Lan, S.-H., Kong, A. K. H., Verbunt, F., Lewin, W. H. G., Bassa, C., Anderson, S. F., & Pooley, D. 2010, ApJ, 712, 380
Lu, T.-N., Kong, A. K. H., Bassa, C., Verbunt, F., Lewin, W. H. G., Anderson, S. F., & Pooley, D. 2009, ApJ, 705, 175
Pooley, D., & Hut, P. 2006, ApJ, 646, L143
Pooley, D., et al. 2002a, ApJ, 573, 184
Pooley, D., et al. 2002b, ApJ, 569, 405
Predehl, P., & Schmitt, J. H. M. M. 1995, A&A, 293, 889
Richer, H. B., et al. 1997, ApJ, 484, 741
Rutledge, R. E., Bildsten, L., Brown, E. F., Pavlov, G. G., & Zavlin, V. E. 2002, ApJ, 578, 405
Servillat, M., et al. 2008, A&A, 490, 641
Shara, M. M., Bergeron, L. E., & Moffat, A. F. J. 1994, ApJ, 429, 767
Smith, R. K., Brickhouse, N. S., Liedahl, D. A., & Raymond, J. C. 2001, ApJ, 556, L91
Tucholke, H., Scholz, R., & Brosche, P. 1996, A&A, 312, 74
Verbunt, F. 2001, A&A, 368, 137
Verbunt, F. 2002, in ASP Conf. Ser. 265, Omega Centauri, A Unique Window into Astrophysics, ed. F. van Leeuwen, J. D. Hughes, & G. Piotto (San Francisco, CA: ASP), 289
Verbunt, F., Bunk, W. H., Ritter, H., & Pfeffermann, E. 1997, A&A, 327, 602
Verbunt, F., Pooley, D., & Bassa, C. 2007, in IAU Symp. 246, Dynamical Evolution of Dense Stellar Systems, ed. E. Vesperini, M. Giersz, & A. Sills (Cambridge: Cambridge Univ. Press), 301